1	Diverging Hydrological Sensitivity among Tropical Basins
2	Jie He ^{1*} , Kezhou Lu ¹ , Boniface Fosu ^{2,3} , Stephan A. Fueglistaler ⁴
3	*Corresponding Author. Contact: jie.he@eas.gatech.edu
4	1. School of Earth and Atmospheric Sciences, Georgia Institute of Technology
5	2. Department of Geosciences, Mississippi State University
6	3. Northern Gulf Institute, Mississippi State University
7	4. Department of Geosciences, Princeton University

9 Abstract

The three tropical basins each play a unique role in the global climate system. The main mechanism by which tropical oceans affect remote climate is the latent heating of local precipitation. Here, we report major differences in hydrological sensitivity (HS, i.e., precipitation change per unit surface warming) among tropical basins. Specifically, the Pacific HS is several times as large as that of the Indian basin, while the Atlantic HS is negative. This results from a thermodynamic amplification of the existing spatial unevenness in relative humidity, with the wettest basin getting wetter and the driest basin getting drier. The diverging basin HS is accompanied with an interbasin repartitioning of latent heating and convective mass fluxes, with far-reaching implications on rainfall and surface temperature over tropical and mid-latitude lands. These results suggest that the previously unrecognized inter-basin differences in HS may contribute substantially to the geographic pattern of anthropogenic climate change.

21 Main Text

22

23

24

25

26

27

28

29

30

31

32

33

34

35

36

37

38

39

40

41

42

43

Tropical oceans affect the global climate mainly because the patterns of atmospheric heating resulting from the condensation associated with tropical precipitation impact the generation and propagation of planetary waves ¹. The remote effects of tropical oceans therefore depend on the location and intensity of precipitation ^{2,3}, and each tropical basin is known for its distinct remote influences. As the climate warms, the tropical mean precipitation is expected to increase ^{4,5}, but it is unclear whether precipitation may change differently among basins. Spatial variations in tropical precipitation changes are driven primarily by the pattern of sea surface temperature (SST) changes. This is often referred to as the "warmer-get-wetter" effect, that is, an increase (decrease) in precipitation where the underlying SST rises faster (slower) than the tropical mean SST ^{6,7} (Figs. 1a, b). However, when driven by a spatially uniform sea surface warming, climate models still simulate spatially uneven precipitation changes (Fig. 1c). The spatial unevenness is particularly noticeable at basin scales, with most of the positive changes occurring in the Pacific basin. This suggests that hydrological sensitivity (HS, i.e., precipitation change per degree surface warming) may differ among tropical basins for reasons that have yet to be identified. The extent and mechanisms of inter-basin differences in HS will be examined in this article. In addition, we provide evidence that the previously unrecognized inter-basin differences in HS have far-reaching implications on the global climate system.

Inter-basin differences in hydrological sensitivity

We examine both basin-scale and regional HS in the three tropical (20°S-20°N) basins, as projected by the models participating the Coupled Model Intercomparison Project phase 6 (CMIP6) ⁸. We start with the basin mean hydrological sensitivity (HS_{mean%}), which is defined as the percentage change in the basin mean precipitation per basin mean SST change. Based on coupled

atmosphere-ocean simulations in a high emission scenario (ssp585, Method), the Pacific HS_{mean%} is 3.6 %/°C, roughly five times as large as the Indian basin HS_{mean%} of 0.76 %/°C, whereas the Atlantic HS_{mean%} is -2.2 %/°C (Fig. 2a). While HS_{mean%} varies substantially among models, the inter-basin differences in HS_{mean%} are robust. Over 90% of the models project the highest HS_{mean%} in the Pacific basin and the lowest HS_{mean%} in the Atlantic basin. Over 70% of the models project the Pacific HS_{mean%} to be more than twice as large as the Indian basin HS_{mean%}, whereas over 80% project negative Atlantic HS_{mean%} (Extended Data Fig. 1b).

Next, we examine the basin average local hydrological sensitivity, HS_{local%}, defined as the percentage change in pointwise precipitation per unit local SST change (unit: %/°C). Since the basin average HS_{local%} can be dominated by regions with low present-day precipitation, we also examine HS_{local%} defined as the actual change in pointwise precipitation per unit local SST change (unit: mm d⁻¹/°C). The inter-basin differences in HS_{local%} and HS_{local} are similar to those in HS_{mean%}, as the basin average HS_{local%} and HS_{local} of the Pacific basin are a few times greater than those of the Indian basin and are negative for the Atlantic basin (Figs. 2b, c). Over 90% of the models project the highest average HS_{local%} in the Pacific basin and the lowest average HS_{local%} in the Atlantic basin; Over 70% project the Pacific basin mean HS_{local%} to be more than twice as large as the Indian basin mean HS_{local%}, whereas over 90% project negative Atlantic mean HS_{local%} (Extended Data Fig. 1c). Similar levels of robustness are found for inter-basin differences in basin mean HS_{local} (Extended Data Fig. 1d).

Impacts of diverging basin hydrological sensitivity on land

Because the three basins warm at approximately the same rate (Extended Data Fig. 1a), the diverging HS means a substantial repartition of precipitation and the associated latent heating among tropical basins. Changes in tropical latent heating are known to affect the global

atmospheric circulation via the generation and propagation of planetary waves ^{1,9,10}. Given the well-established significance of tropical heating in the global climate system, the inter-basin repartition of precipitation may be expected to have far-reaching implications. We study the remote impacts of inter-basin differences in HS by perturbing tropical oceanic diabatic heating in the Community Atmosphere Model 5.0 (CAM5) ¹¹. In the first experiment named amipTRP, the impacts of the projected TRoPical oceanic precipitation changes are simulated by adding diabatic heating anomalies produced from the CMIP6 multi-model mean precipitation changes (Fig. 3a). In the second experiment named amipTRPadj, we remove the inter-basin differences in HS_{local%} from amipTRP by applying in each basin a uniform HS_{local%} perturbation, which is set to the difference between the tropical oceanic mean HS_{local%} and the basin mean HS_{local%} (Fig. 3b). Thus, impacts of the inter-basin differences in HS_{local%} are represented by the difference between amipTRP and amipTRPadj. Details of the experiment setup are documented in the Method section.

The CMIP6 projected tropical oceanic precipitation changes have widespread impacts on precipitation over tropical and mid-latitude lands (Fig. 3d). Land responses in the simulation with inter-basin differences in HS_{local%} (amipTRP, Fig. 3d) are generally larger than those without (amipTRPadj, Fig. 3e), indicating that much of these impacts can be attributed to the inter-basin differences in HS_{local%} (Fig. 3f). The remote influences of diverging basin HS_{local%} are most evident in regions surrounding the Atlantic basin. Specifically, the inter-basin differences in HS_{local%} increase precipitation in the continental US, southern parts of South America, and to a lesser degree, northern Europe. They also reduce precipitation in Mexico, the Amazon rainforest, and southern Africa. These changes are largely consistent in sign with the CMIP6 multi-model mean changes (Fig. 3a) and the IPCC best estimate of precipitation changes under ssp585 (cf. Figure 4.42 in IPCC, 2021 ¹²). This suggests that the inter-basin differences in HS_{local%} are a significant

contributor to the projected land precipitation changes. The inter-basin differences in HS_{local%} also affect land surface temperature changes (Extended Data Fig. 2). These results suggest that the diverging basin HS may substantially influence the pattern of climate change over land. Mechanisms of the CAM5 precipitation responses are examined in detail in Supplementary Text 1 with Supplementary Figures 1-5.

Mechanisms for diverging basin hydrological sensitivity

We investigate the mechanisms for the inter-basin differences in $HS_{mean\%}$. The inter-basin differences in $HS_{local\%}$ and HS_{local} are both significantly correlated with those in $HS_{mean\%}$ (Extended Data Fig. 3), indicating that their mechanisms may be related.

Spatial variations in tropical precipitation changes are often attributed to the pattern of the underlying SST changes according to the "warmer-get-wetter" theory ⁶. However, the inter-basin differences in precipitation changes occur despite similar surface warming across basins (Extended Data Fig. 1a). By comparing atmospheric model responses to spatially uniform and structured sea surface warming (with experiment names of amipUniform and amipAll, respectively, see Method), we find that the pattern of SST changes does not substantially affect the inter-basin differences in HS (Figs. 2a-c).

The "warmer-get-wetter" theory is a two-step argument. First, the relatively uniform tropical upper tropospheric temperature makes boundary-layer moist static energy (MSE0) the main driver of atmospheric instability ^{13,14}. Second, SST becomes the main driver of MSE0 changes and ultimately, precipitation changes, when spatial variations in relative humidity changes are negligible ^{6,15}. To understand why the "warmer-get-wetter" theory fails at the basin scale, we evaluate both parts of the theory by examining basin precipitation as a function of relative SST

(SST $_{rel}$, defined as SST minus the tropical mean SST) and MSE0 (calculated as pressure weighted MSE averaged between 1000 - 850 hPa).

We first examine basin precipitation in relative SST_{rel} space (Figs. 4a, b). At present-day, inter-basin differences in precipitation-SST relationships already exist, with the Pacific being the most favorable for precipitation at a given SST. This is true for both models and observations (Method), albeit to a lesser degree in the latter. As the climate warms, such inter-basin differences are projected to intensify (Fig. 4a). Specifically, the Pacific precipitation increases markedly throughout the convective regime, except at very high SST_{rel}. The Indian Ocean precipitation is largely unchanged except increasing moderately near -1.5 °C SST_{rel}. The Atlantic precipitation decreases moderately over most of the SST_{rel} range. Contrary to previous belief ¹⁶, the inter-basin differences in precipitation and precipitation changes in SST_{rel} space suggest that SST_{rel} is not a good predictor of the present or future precipitation. As we show next, these differences are key to understanding the diverging basin HS.

In Figures 4c and 4d, we examine precipitation as a function of the relative MSE0 (MSE0_{rel}). As detailed in Method, MSE0_{rel} is calculated as MSE0 normalized by the tropical mean MSE0. (Changes in the latter have little effect on precipitation ¹⁷ and are thus removed through normalization.) Despite the apparent conundrum in SST_{rel} space, precipitation is much more consistent among basins and between present and future simulations, when it is expressed as a function of MSE0_{rel}. This means that the inter-basin discrepancies in precipitation at a given SST_{rel} are largely caused by the inter-basin discrepancies in MSE0_{rel}. Because changes in boundary-layer temperature are similar across basins (Extended Data Fig. 4), we can further attribute the interbasin differences in MSE0_{rel} to differences in boundary-layer relative humidity (RH0, calculated as pressure weighted relative humidity averaged between 1000 – 850 hPa). The present-day RH0

is highest in the Pacific basin in both models and reanalyses (Method, Figs. 4e, f). Upon warming, RH0 is projected to further increase in the Pacific basin, and further decrease in the Atlantic basin. In the Indian basin, RH0 increases around -1.5 °C SST_{rel}. These changes in RH0 are consistent with those in precipitation (Fig. 4a).

Thus, to understand the diverging basin HS, we need to understand why RH0 differs among basins at given SSTs and why such differences are amplified under warming. The inter-basin differences in the present-day RH0 are explained in detail in Supplementary Text 2 with Supplementary Figures 6 and 7. To summarize, spatial variations in RH0 are largely determined by boundary-layer moisture transport (TRP0, Method). Large portions of the Indian and Atlantic basins are located downwind of arid lands, which makes these basins more susceptible to the advection of dry air. In addition, the sharp SST fronts in the northeastern Pacific drive large boundary-layer moisture convergence, which is largely absent in the other basins. The lack of dry advection and the presence of strong moisture convergence combine for a net moisture import in the Pacific boundary layer (i.e., a positive Pacific basin mean TRP0), whereas the opposite is true for the Atlantic basin (Fig. 2e). As a result, the Pacific basin has higher RH0 at given SSTs, which results in greater MSE0 and ultimately, larger precipitation.

Next, we analyze the projected TRP0 changes (Fig. 2f), which are dissected into a thermodynamic component driven by the atmospheric moistening and a dynamic component driven by boundary-layer circulation changes (Method). As the climate warms, the increasing moisture concentration intensifies the existing pattern of moisture transport ¹⁸. This leads to positive changes in moisture transport for regions with net moisture import and the opposite for regions with net moisture export – commonly referred to as "wet-get-wetter and dry-get-drier". Consistent with this view, we find positive thermodynamic TRP0 changes in the Pacific basin and

negative changes in the Atlantic basin. This leads to an intensification of the existing inter-basin differences in TRP0, as the dynamic TRP0 changes are similar across basins. The intensification of inter-basin differences in TRP0 explains the diverging basin RH0 changes. Furthermore, it explains why MSE0 changes differently among basins, despite similar SST changes. The connection among changes in TRP0, RH0, and MSE0 can also be appreciated at regional scales, as the three variables bear a high degree of spatial resemblance (Extended Data Fig. 5).

MSE0 affects precipitation via its influences on the convective mass flux, as strong convection tends to occur in regions of high MSE0 ¹⁴. While the convective mass flux is projected to weaken ¹⁹, the inter-basin differences in MSE0 changes suggest that it may not weaken at the same rate among basins. We calculate convective mass flux at each model grid point as precipitation divided by local surface specific humidity following ref. 20, and compare this method with calculations based on vertically integrated convective mass flux from a subset of models that provide such output (Supplementary Table 1). The rate of convection weakening is largest in the Atlantic basin and smallest in the Pacific basin (Fig. 2d). This is inversely correlated with the MSE0 changes in each basin, as expected from theoretical relationships between convection and MSE0 ¹⁵. Over 90% of the CMIP6 models project the largest weakening in the Atlantic basin and the least weakening in the Pacific basin. Roughly 70% of the models project the Atlantic basin mean weakening rate to be more than twice as large as that of the Pacific basin (Extended Data Fig. 1e).

Discussion

Spatial variations in tropical precipitation changes are expected to follow the pattern of SST changes. But as the climate warms, the increasing inter-basin disparities in RH0 make SST a less accurate proxy for MSE0 and consequently, a bad predictor of precipitation changes at basin

scales. At regional scales, the sensitivity of precipitation to warming is set by relative humidity, which is demonstrated by the spatial resemblance between HS_{local%} and RH0 changes (Extended Data Fig. 5). Therefore, spatial variations in RH0 not only cause HS to diverge among basins, but is important for the spatial variation in oceanic precipitation changes in general. This is particularly evident in the amipUniform simulation, where spatial variations in RH0 cause uneven changes in MSE0_{rel}, which lead to spatially varying precipitation changes despite a uniform surface warming (Extended Data Figs. 5a, c, e).

Our results show that the diverging HS is rooted in the thermodynamic intensification of boundary-layer moisture transport. The thermodynamic origin is likely the reason the diverging basin HS is robustly projected by models. While the fidelity of the state-of-the-art precipitation projections has been questioned ²¹, the thermodynamic intensification of moisture transport has been confirmed by observations ²². This suggests that the diverging basin HS is likely a reliable projection. On the other hand, the extent to which HS diverges among basins varies among models, and such variation is closely tied to inter-model variations in the thermodynamic intensification of the present-day TRP0 (Extended Data Fig. 6). Therefore, model biases in the present-day TRP0 likely contribute to the quantitative disagreement on the inter-basin differences in HS.

Acknowledgement

We thank Dr. Isla Simpson and Dr. Mingfang Ting for helping with the CAM5 and stationary wave model simulations and Dr. Jean Lynch-Stieglitz for helping with the writing of the manuscript. J.H. is supported by the National Science Foundation (NSF) grant AGS-2047270 and B.F. is supported by NSF grant AGS-2217619. We acknowledge the World Climate Research Programme's Working Group on Coupled Modelling, which is responsible for CMIP, and we thank the climate modelling

groups for producing and making available their model output. For CMIP, the US Department of Energy's Program for Climate Model Diagnosis and Intercomparison provides coordinating support and led development of software infrastructure in partnership with the Global Organization for Earth System Science Portals. We acknowledge the CESM Large Ensemble Community Project and supercomputing resources provided by NSF, the National Center for Atmospheric Research (NCAR), and Yellowstone. We thank the Physical Sciences Laboratory (PSL) of the National Oceanic and Atmospheric Administration and the Goddard Earth Sciences Data and Information Services Center for providing precipitation observations. We thank the Copernicus program, PSL, and NCAR for providing the reanalysis data.

Author contributions statement

J.H. designed the study and led the writing of the manuscript. J.H. analyzed the diverging basin hydrological sensitivity, and K.L. conducted and analyzed the diabatic heating experiments. B.F. and S.A.F. contributed to the analysis. All authors contributed to scientific interpretation and the

Competing interests statement

writing of the manuscript.

The authors declare no competing interests.

Figures

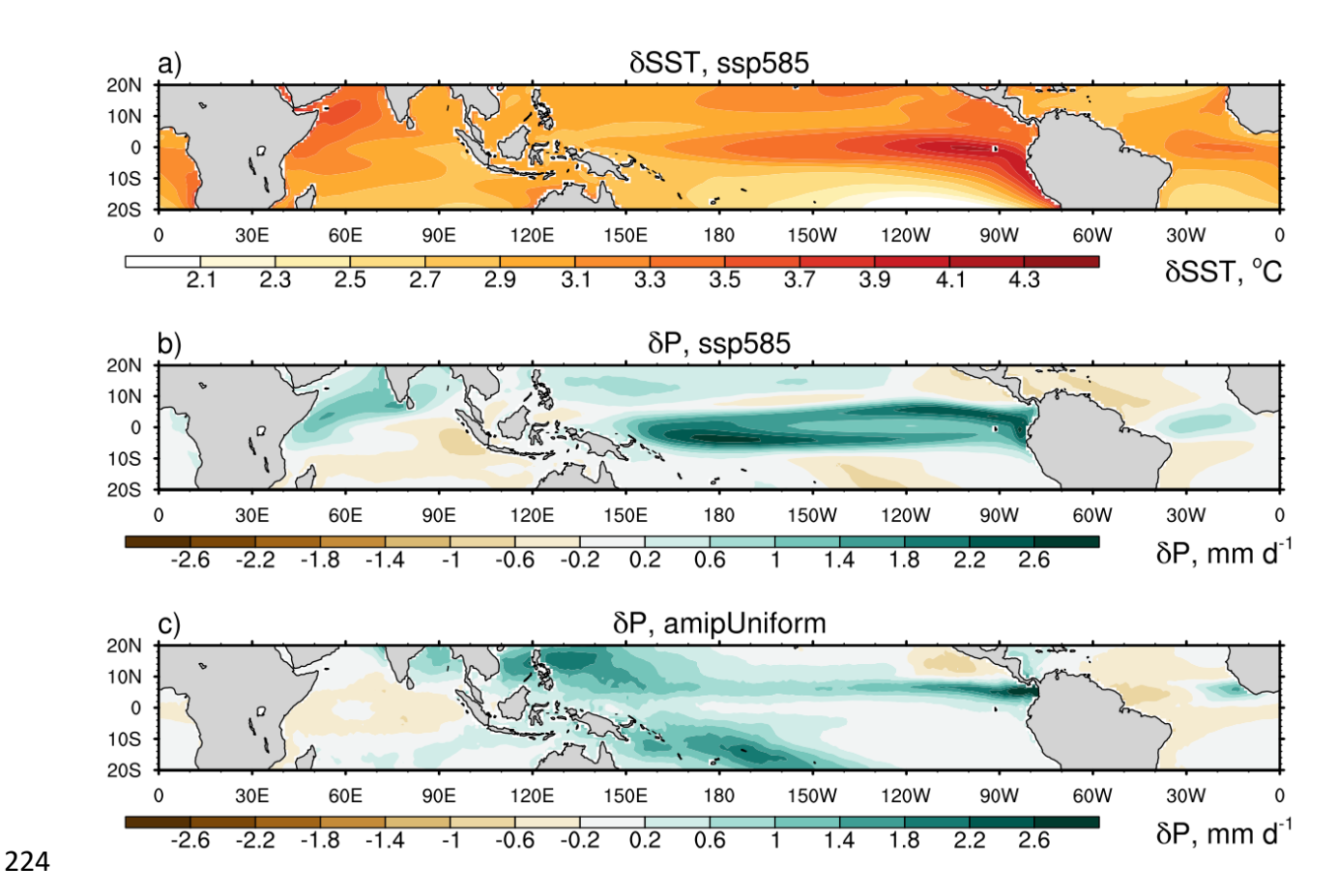


Figure 1. Tropical changes from structured and uniform sea surface warming. a-b) Multi-model mean SST (a) and precipitation (b) changes from the CMIP6 ssp585 simulation. c) Multi-model mean precipitation changes from amipUniform, which contains an elevated CO₂ concentration and a uniform sea surface warming relative to its baseline simulation (see Method).

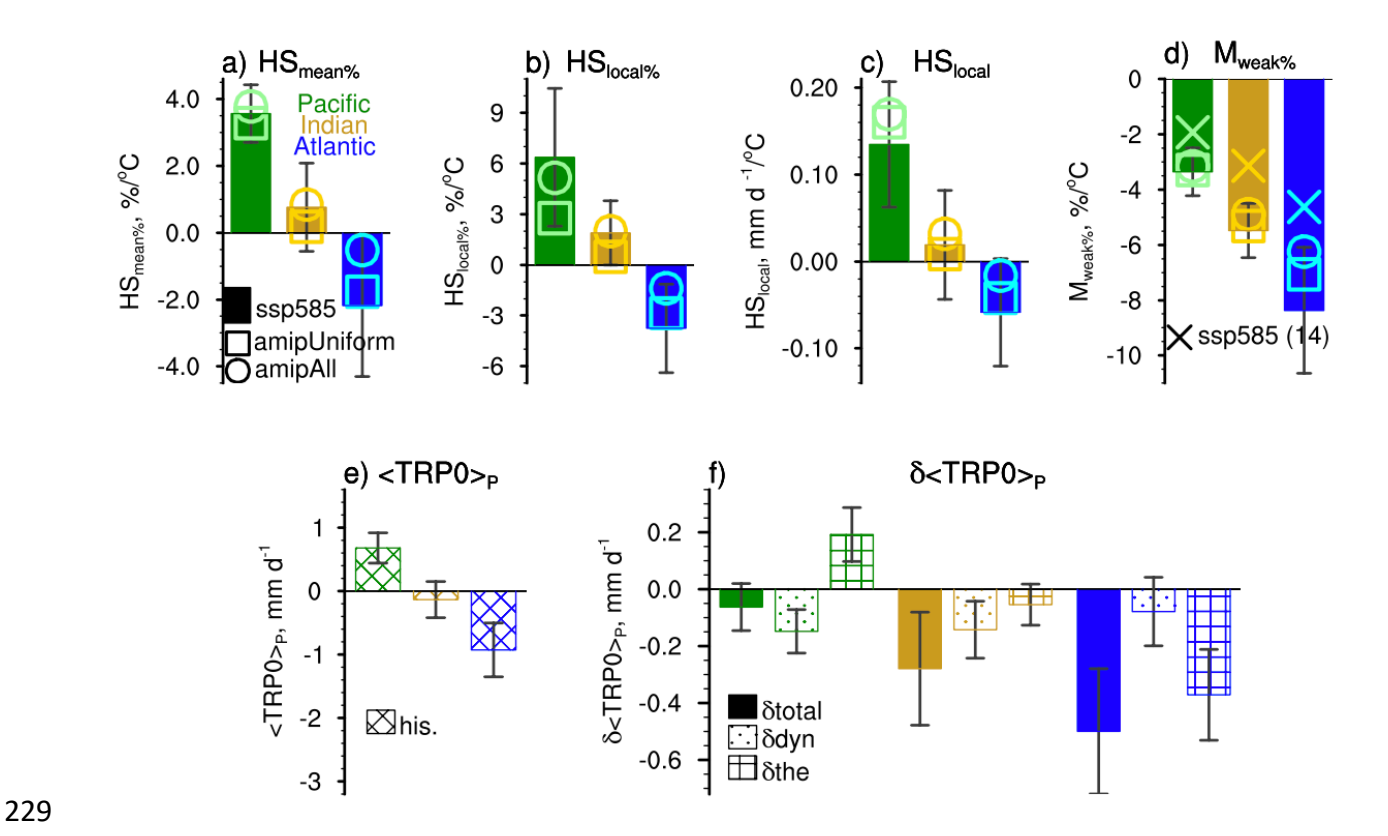


Figure 2. Inter-basin differences in hydrological sensitivity. a-d) CMIP6 multi-model mean HS_{mean%} (a), basin average HS_{local%} (b), basin average HS_{local} (c), and percentage change in basin average convective mass flux, M_{weak%} (d) from the ssp585, amipUniform, and amipAll simulations. In panel (d), convective mass flux is calculated at each grid point as precipitation divided by local surface specific humidity, except symbol ×, which is calculated by using models' actual convective mass flux integrated from surface to the top of the atmosphere from the 14 models that provide convective mass flux output.

e) Present-day basin mean TRP0 from the historical simulation. f) Future changes in total and individual components of basin mean TRP0 from the ssp585 simulation. δtotal, δdyn, and δthe denote the total, dynamic, and thermodynamic changes, respectively. In panels (e) and (f), TRP0 is weighted by the local climatological precipitation before it is averaged over basins. Weighting is applied to focus on convective areas, thus making the basin average TRP0 more relevant to precipitation. Bars represent the multi-model mean, whereas whiskers represent one inter-model standard deviation.

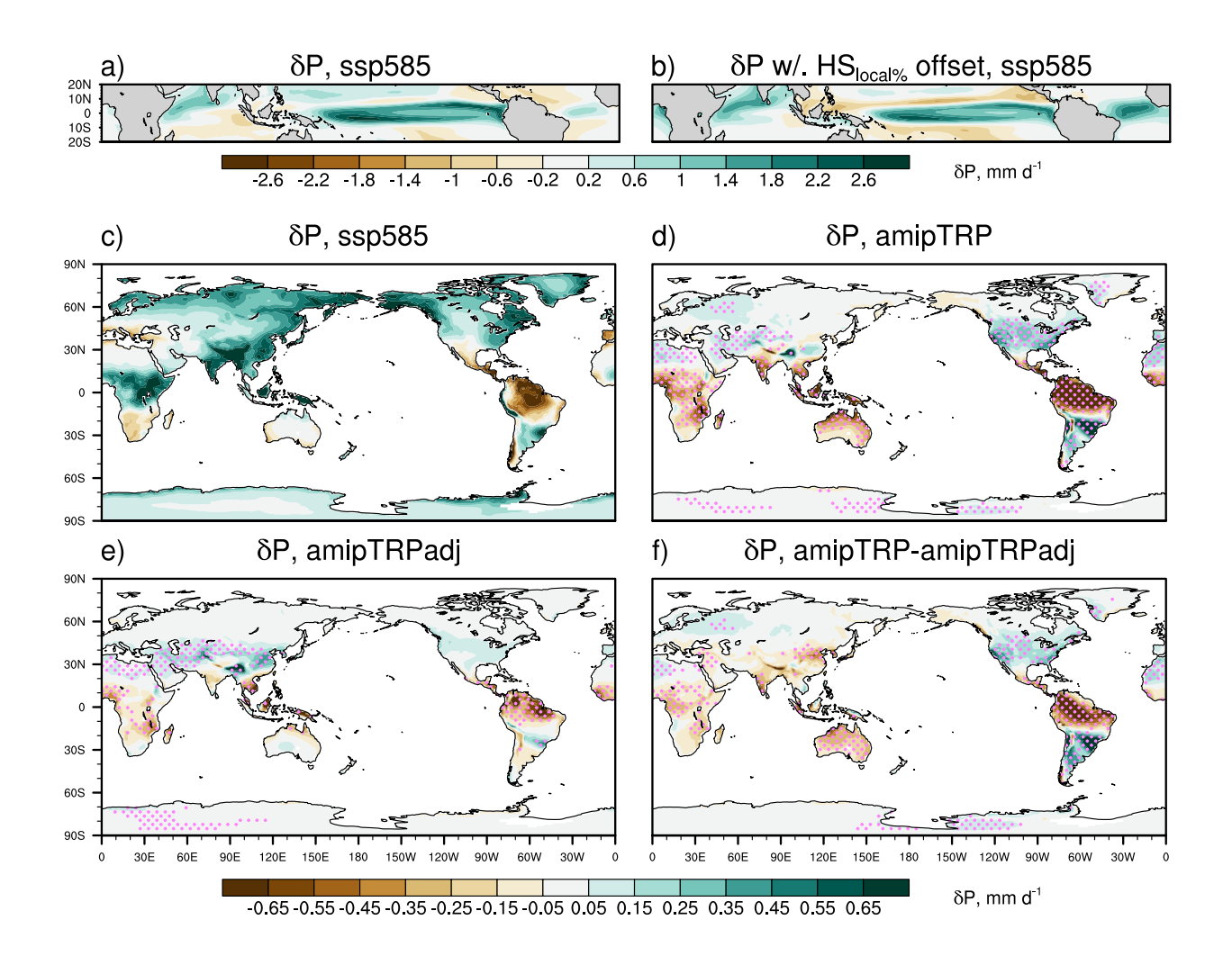


Figure 3. Diverging basin hydrological sensitivity and its impacts on land precipitation. a) Oceanic precipitation changes from the CMIP6 multi-model mean ssp585 simulation. b) Same as panel (a) but with inter-basin differences in the basin mean HS_{local%} removed. c) Future changes in land precipitation from the CMIP6 multi-model mean ssp585 simulation. d-f) Land precipitation responses in amipTRP (d), amipTRPadj (e), and the difference between amipTRP and amipTRPadj (f). In panels (d-f), regions where precipitation responses are significantly above internal variability (Method) are stippled.

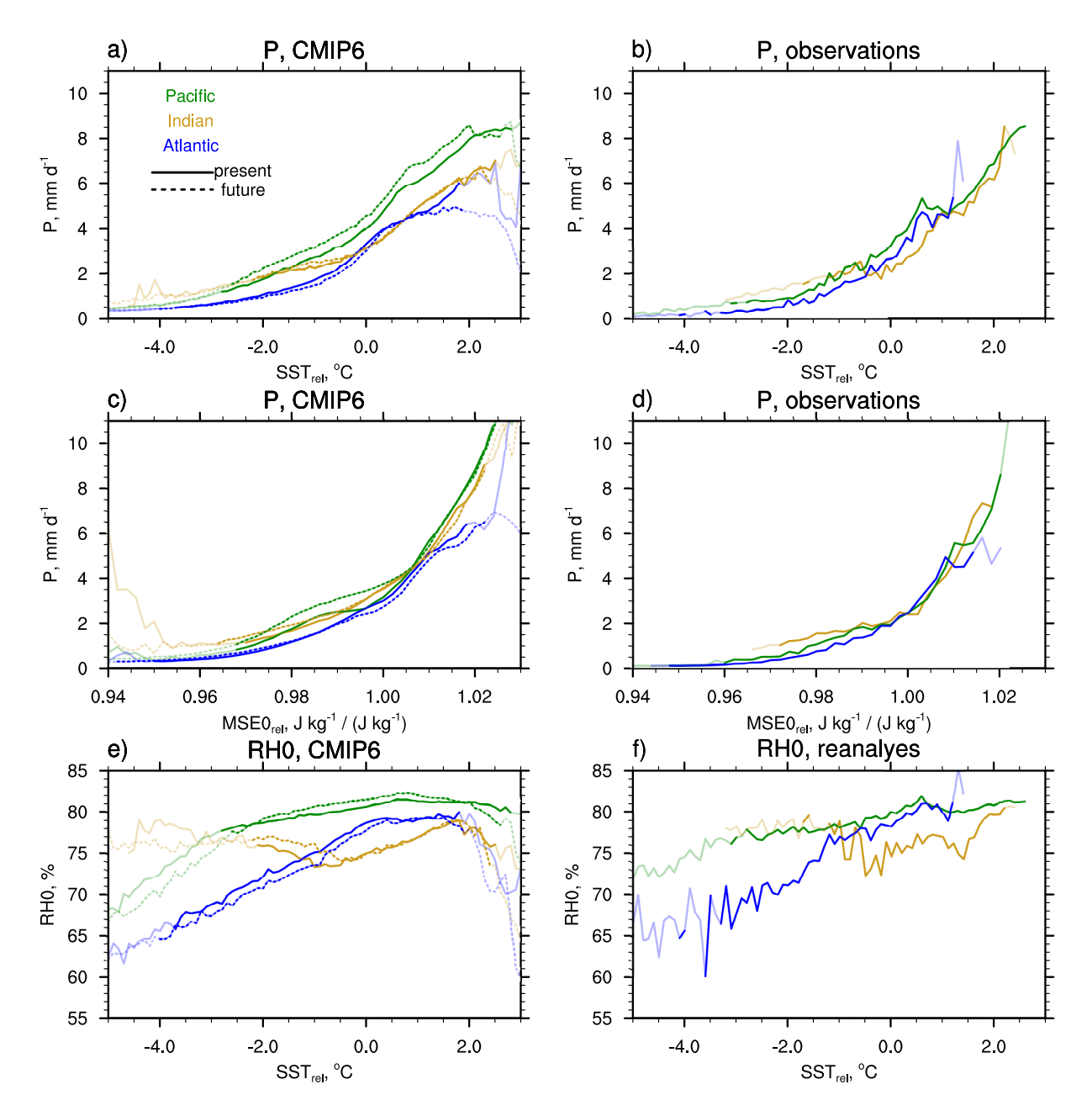


Figure 4. Factors of precipitation and precipitation change. a) Multi-model mean present and future precipitation averaged for 0.1 °C SST_{rel} bins for individual basins. b) Observed precipitation averaged as in panel (a). c-d) Same as panels (a) and (b) except for precipitation averaged for 0.002 MSE_{rel} bins. e) Multi-model mean present and future RH0 averaged for 0.1 °C SST_{rel} bins. f) Present RH0 from reanalyses averaged as in panel (e). In panels (a), (b), (e), and (f), SST_{rel} bins that account for less than 0.5% of the total basin area are shown in semitransparent colors; the same is applied in

- panels (c) and (d) for MSE_{rel} bins that account for less than 0.5% of the total basin area. Simulated present and future conditions are taken from the historical and ssp585 simulations, respectively.
- 259

References

- 261 1. Trenberth, K. E. et al. Progress during TOGA in understanding and modeling global
- teleconnections associated with tropical sea surface temperatures. J. Geophys. Res. 103,
- 263 14291–14324 (1998).
- 264 2. Barsugli, J. J. & Sardeshmukh, P. D. Global Atmospheric Sensitivity to Tropical SST Anomalies
- throughout the Indo-Pacific Basin. *J. Climate* **15**, 3427–3442 (2002).
- 266 3. Zhang, S., Stier, P., Dagan, G., Zhou, C. & Wang, M. Sea surface warming patterns drive
- 267 hydrological sensitivity uncertainties. *Nature Climate Change* 1–9 (2023).
- 4. Allan, R. P., Soden, B. J., John, V. O., Ingram, W. & Good, P. Current changes in tropical
- precipitation. *Environmental Research Letters* **5**, 025205 (2010).
- 5. Tan, J., Jakob, C., Rossow, W. B. & Tselioudis, G. Increases in tropical rainfall driven by
- 271 changes in frequency of organized deep convection. *Nature* **519**, 451–454 (2015).
- 272 6. Xie, S.-P. et al. Global Warming Pattern Formation: Sea Surface Temperature and Rainfall. J.
- 273 *Climate* **23**, 966–986 (2010).
- 7. Duffy, M. L., O'Gorman, P. A. & Back, L. E. Importance of Laplacian of Low-Level Warming for
- the Response of Precipitation to Climate Change over Tropical Oceans. *Journal of Climate*
- **33**, 4403–4417 (2020).
- 277 8. Eyring, V. et al. Overview of the Coupled Model Intercomparison Project Phase 6 (CMIP6)
- 278 experimental design and organization. Geoscientific Model Development 9, 1937–1958
- 279 (2016).

- 280 9. Stan, C. et al. Review of tropical-extratropical teleconnections on intraseasonal time scales.
- 281 *Reviews of Geophysics* **55**, 902–937 (2017).
- 10. Yuan, X., Kaplan, M. R. & Cane, M. A. The interconnected global climate system—A review
- of tropical–polar teleconnections. *Journal of Climate* **31**, 5765–5792 (2018).
- 284 11. Neale, R. B. et al. Description of the NCAR community atmosphere model (CAM 5.0). NCAR
- 285 *Tech. Note NCAR/TN-486+ STR* **1**, 1–12 (2010).
- 12. Lee, J.-Y. et al. Future global climate: scenario-based projections and near-term information.
- in Climate change 2021: The physical science basis. Contribution of working group I to the
- 288 sixth assessment report of the intergovernmental panel on climate change 553–672
- 289 (Cambridge University Press, 2021).
- 290 13. Sobel, A. H., Nilsson, J. & Polvani, L. M. The weak temperature gradient approximation and
- balanced tropical moisture waves. *Journal of the atmospheric sciences* **58**, 3650–3665
- 292 (2001).
- 293 14. Zhang, Y. & Fueglistaler, S. How tropical convection couples high moist static energy over
- land and ocean. *Geophysical Research Letters* **47**, e2019GL086387 (2020).
- 295 15. Neelin, J. D. & Held, I. M. Modeling Tropical Convergence Based on the Moist Static Energy
- 296 Budget. Mon. Wea. Rev. 115, 3–12 (1987).
- 297 16. Johnson, N. C. & Xie, S.-P. Changes in the sea surface temperature threshold for tropical
- 298 convection. *Nature Geosci* **3**, 842–845 (2010).
- 299 17. Williams, I. N., Pierrehumbert, R. T. & Huber, M. Global warming, convective threshold and
- false thermostats. *Geophysical Research Letters* **36**, (2009).

301	18. Held, I. M. & Soden, B. J. Robust responses of the hydrological cycle to global warming. J.
302	Climate 19 , 5686–5699 (2006).
303	19. Vecchi, G. A. & Soden, B. J. Global warming and the weakening of the tropical circulation. J.
304	Climate 20 , 4316–4340 (2007).
305	20. Chadwick, R., Boutle, I. & Martin, G. Spatial patterns of precipitation change in CMIP5: why
306	the rich do not get richer in the tropics. J. Climate 26, 3803–3822 (2013).
307	21. Fiedler, S. et al. Simulated tropical precipitation assessed across three major phases of the
308	Coupled Model Intercomparison Project (CMIP). Monthly Weather Review 148, 3653–3680
309	(2020).
310	22. Yu, L., Josey, S. A., Bingham, F. M. & Lee, T. Intensification of the global water cycle and
311	evidence from ocean salinity: a synthesis review. Annals of the New York Academy of
312	Sciences 1472 , 76–94 (2020).
313	
314	
315	Methods
316	Data
317	CMIP6
318	We analyze coupled and atmosphere-only simulations in CMIP6 8 by drawing models that
319	provide all necessary variables. We use one realization from each model, as listed in
320	Supplementary Table 1. All model outputs are interpolated onto a common 1° by 1° grid.
321	We use 1985-2014 of the historical simulation to define the present-day condition, 2071-
322	2100 of the ssp585 simulation to define the future condition, and the difference between the latter

and former to define future changes. The ssp585 simulation represents the upper boundary of the

range of emission scenarios included in CMIP6, and its radiative forcing reaches 8.5 W/m² by 2100. Forty-six models are analyzed. When calculating local hydrological sensitivity (i.e., $HS_{local\%}$ and HS_{local}), we ignore grid points with negative SST changes (which account for less than 0.01% of all model grid points in the ssp585 simulation).

324

325

326

327

328

329

330

331

332

333

334

335

336

337

338

339

340

341

342

343

344

345

346

To understand the impact of the pattern of SST changes, we apply four uncoupled atmosphere-only simulations: 1) amip, driven by historical forcing and observed SST and sea ice concentration from 1979 to 2014, 2) amip4xCO2, which is the same as amip except that CO₂ concentration is quadrupled, 3) amip4K, which is the same as amip but with additional 4 °C SST across global oceans, and 4) amipFuture, which is the same as amip4K but with spatially varying SST anomalies. The spatially varying SST anomalies are taken from the CMIP3 multi-model SST responses to 4xCO₂ in the coupled 1pctCO₂ simulation (where the atmospheric CO₂ concentration increases by 1% per year starting from the pre-industrial level), which are then scaled to have a global mean SST anomaly of 4 °C ²³. We use amip as our baseline (i.e., the present-day control run). Changes in amip4K and amipFuture are scaled to obtain responses at 4×CO₂, by dividing changes by each model's tropical mean SST change in amip4K and amipFuture, respectively and then multiplying them by each model's tropical mean SST change at 4×CO₂ from the coupled 1pctCO2 simulation. To obtain SST changes at 4×CO₂ from 1pctCO2, we calculate SST changes between the last and first 30 years (121-150 minus 1-30) of the simulation, and then scale them by log(4)/log(1.01¹²⁰) assuming that the SST changes are proportional to the logarithm of CO₂ changes. Because changes from the direct CO₂ forcing and SST increase are linearly additive ²⁴, we create amipUniform by summing changes in amip4xCO2 and the scaled changes in amip4K, and amipAll by summing changes in amip4xCO2 and the scaled changes in amipFuture. Eleven uncoupled models are analyzed.

Observations

Our SST data is a merged product based on the Hadley Centre SST dataset version 1 and the National Oceanic and Atmospheric Administration optimum interpolation SST analysis version 2 ²⁵. The data ranges from 1979 to 2021 and is archived at 1° resolution. This SST dataset was also used as the boundary condition for the CMIP6 amip simulation.

To account for the uncertainty among precipitation datasets, we average three widely used precipitation datasets: 1) GPCP (the Global Precipitation Climatology Project) version 2 ²⁶ from 1979 to 2021 at 2.5° resolution, 2) CMAP (the Climate Prediction Center Merged Analysis of Precipitation) ²⁷ from 1979 to 2021 at 2.5° resolution, and 3) TRMM (the Tropical Rainfall Measuring Mission Project) 3B43 version 7 ²⁸ from 1998 to 2019 at 0.25° resolution. In all three datasets, oceanic precipitation is derived from satellites. The multi-observation mean features discussed in this paper are generally present in individual datasets as well. All observational data are interpolated onto the same 1° by 1° grid that is used for interpolating CMIP6 outputs.

Reanalysis Data

We analyze monthly air temperature, specific humidity, relative humidity, winds, and geopotential height from reanalysis data during the period of 1979 to 2021. To minimize the effect of uncertainty within individual datasets, we average three widely used reanalyses: 1) ERA5 (the 5th generation of the European Centre for Medium-Range Weather Forecasts reanalysis) ²⁹ on a 30km horizontal grid and 137 vertical levels, 2) NCEP/DOE-II (the National Center for Environmental Prediction and Department of Energy Reanalysis II) ³⁰ at 2.5° resolution with 17 vertical levels, and 3) JRA-55 (the Japanese 55-year Reanalysis) ³¹ at roughly 1° resolution with 37 vertical levels. The multi-dataset mean features presented in this paper are generally found in

individual reanalysis as well. All reanalysis data are interpolated onto the same 1° by 1° grid that is used for interpolating CMIP6 outputs.

Relative boundary-layer moist static energy

We analyze the relationship between precipitation and MSE0 in individual basins, but present MSE0 in its normalized form (i.e., MSE0 divided by the tropical ocean mean MSE0), which we refer to as the relative boundary-layer moist static energy (MSE0_{rel}). MSE0_{rel} allows for direct comparisons between present and future MSE-precipitation relationships, by dismissing changes in the tropical mean MSE0 (which has little practical effect on precipitation due to the upper-tropospheric warming ¹⁷). In addition, the nonlinear Clausius-Clapeyron relationship automatically makes MSE0 more spatially uneven with warming ³². We discount the effect of the Clausius-Clapeyron amplification of the spatial unevenness in MSE0 by removing the tropical mean MSE0 through scaling rather than shifting (the latter is used for defining SST_{rel}). Therefore, changes in the spatial unevenness in MSE0_{rel} are either due to changes in the spatial unevenness in boundary-layer temperature or those in boundary-layer relative humidity. As explained in the main text, it is the latter that intensifies the inter-basin discrepancies in MSE0_{rel}.

Boundary-layer moisture transport

TRP0 is calculated at each tropical ocean grid point as:

386
$$TRP0 = -\int_{1000 \ hPa}^{850 \ hPa} (\vec{V} \cdot \nabla q) dp - \int_{1000 \ hPa}^{850 \ hPa} (q \cdot \nabla \vec{V}) dp - \int_{1000 \ hPa}^{850 \ hPa} \left[\frac{\partial (\omega \cdot q)}{\partial p} \right] dp \qquad (1)$$

where \vec{V} is horizontal wind velocity, q is specific humidity, ω is pressure velocity, and p is pressure.

The first term on the right-hand side is the transport due to horizontal advection. The second and

third terms are both driven by boundary-layer wind convergence, and we refer to the sum of the

second and third terms as the convergence term.

Changes in TRP0 can be decomposed into a thermodynamic component, $-\int_{1000 \ hPa}^{850 \ hPa} (\vec{V} \cdot \vec{V}) dp - \int_{1000 \ hPa}^{850 \ hPa} (\delta q \cdot \nabla \vec{V}) dp - \int_{1000 \ hPa}^{850 \ hPa} \left[\frac{\partial (\omega \cdot \delta q)}{\partial p} \right] dp$ and a dynamic component, $-\int_{1000 \ hPa}^{850 \ hPa} (\delta \vec{V} \cdot \nabla q) dp - \int_{1000 \ hPa}^{850 \ hPa} (q \cdot \nabla \delta \vec{V}) dp - \int_{1000 \ hPa}^{850 \ hPa} \left[\frac{\partial (\delta \omega \cdot q)}{\partial p} \right] dp$, where δ denotes future changes.

CAM5 Experiments with perturbed diabatic heating

Tropical precipitation drives global teleconnections through planetary Rossby waves generated from the release of latent heat. We examine how tropical inter-basin HS divergence affects land precipitation via a series of atmosphere-only experiments with perturbed diabatic heating. The model used here is the Community Atmosphere Model, version 5 (CAM5) within the framework of the Community Atmosphere Model, version 1 (CESM1 ³³), at a horizontal resolution of 1 degree. The baseline simulation is driven by pre-industrial forcing and monthly SST and sea ice concentrations of a 2600-year CESM1 pre-industrial control simulation (available via the CESM1 large ensemble ³⁴).

We apply two types of diabatic heating perturbation in tropical oceanic regions on top of the baseline simulation. In the first experiment (named amipTRP), the diabatic heating perturbation is produced from the CMIP6 multi-model mean tropical oceanic precipitation change in ssp585 (Fig. 3a). In the second experiment (named amipTRPadj), we apply the same diabatic heating perturbation as amipTRP but with inter-basin discrepancies in HS_{local%} removed. Specifically, we add the difference between the tropical oceanic mean HS_{local%} and the basin mean HS_{local%} uniformly to the HS_{local%} at all grid points in each basin and in each CMIP6 model. We then use the adjusted HS_{local%} and the climatological precipitation and SST changes in each model

to recalculate the tropical oceanic precipitation change, δP_{adj}. The multi-model mean δP_{adj} (Fig. 3b)
 is used to produce the diabatic heating perturbation in amipTRPadj.

To obtain the diabatic heating perturbations from precipitation changes, we assume that models' diabatic heating has an idealized Gaussian vertical profile that peaks at 400 hPa 35,36 . This allows us to approximate the target diabatic heating (δQ_T) as

417
$$\delta Q_T(p, lat, lon) = C_s \delta P(lat, lon) e^{-\frac{(p-p_c)^2}{2r^2}}$$
 (2)

where C_s is a scaling constant and is set to 162.92 m² s⁻², P is precipitation, p is pressure and p_c is set to 400 hPa, r is the decaying radius and is set to 3.

The diabatic heating perturbation is added to CAM5 as a seasonally varying constant temperature tendency term at the end of each physics time step. Because model's diabatic heating is free to respond to the perturbation, the total diabatic heating anomaly deviates from the prescribed diabatic heating perturbation. To match the model's actual diabatic heating with δQ_T , we determine the prescribed diabatic heating forcing through an "iterative approach" detailed in ref ³⁷. Each iteration ensemble (*i*) contains ten members of three-year runs that branch off from various years of the baseline simulation. The diabatic heating perturbation is calculated as

427
$$\delta Q(i) = \begin{cases} C \cdot \delta Q_T, & \text{for } i = 1\\ \delta Q(i-1) + C \cdot \left(\delta Q_T - \frac{1}{10} \sum_{n=1}^{10} (\delta Q(i-1) + \delta Q_n(i-1))\right), & \text{for } 2 \le i \le 10 \end{cases}$$
(3)

where $\delta Q(i-1) + \delta Q_n(i-1)$ is the actual diabatic heating anomaly in ensemble member n of iteration i-1, which contains the prescribed diabatic heating forcing $\delta Q(i-1)$ and the model's diabatic heating response to such forcing $\delta Q_n(i-1)$. With each iteration, the model's actual diabatic heating anomaly is pulled towards the target diabatic heating anomaly by adding a diabatic heating perturbation which is equal to C times the difference between the target diabatic heating anomaly and the model's actual diabatic heating anomaly. C is set to 0.25 for $i \le 7$ and 0.15 for i > 7. C is smaller than

1 because the model's diabatic heating response tends to be in the same sign as and several times larger than the prescribed diabatic heating forcing. As a result, using a smaller C allows the model to reach the target diabatic heating anomaly with fewer iteration ensembles. The final diabatic heating perturbation is obtained after ten iterations ($\delta Q(10)$), which is then applied in amipTRP and amipTRPadj. The simulated vertically integrated diabatic heating anomalies in amipTRP and amipTRPadj (Supplementary Fig. 8) are reasonably close to the target precipitation anomalies (Figs. 3a, b). The amipTRP, amipTRPadj, and the baseline simulations are all 30-year long.

Baroclinic Stationary Wave Model

We investigate the CAM5 simulations by comparing the CAM5 circulation responses to those generated in a Stationary Wave model (SWM). The SWM is a nonlinear baroclinic model that has been widely used to study stationary wave responses to diabatic heating forcings ^{38,39}. The SWM does not include model physics, such as cloud, radiation, and precipitation and is thus not susceptible to issues associated with parameterizations. The SWM is a perturbation model, where only deviations from the climatology is calculated. The model is based on the three-dimensional primitive equations. The numerical stability of the SWM is achieved through an idealized damping and the relaxation towards a specified basic state. The basic state is prescribed as the three-dimensional annual-mean climatology including winds and temperature, derived from the CAM5 control simulation. The diabatic heating perturbation is added to SWM as a constant temperature tendency term.

Three experiments are conducted – 1) SWM-TRP, where the diabatic heating perturbation is produced from the CMIP6 multi-model mean precipitation changes (Fig. 3a) and is the same as that in amipTRP; 2) SWM-TRPadj, where diabatic heating perturbation is produced from the CMIP6 multi-model mean precipitation changes but with the inter-basin differences in HS_{local%}

removed (Fig. 3b) and is the same as that in amipTRPadj; 3) SWM-TRP-d-TRPadj, where diabatic heating perturbation is produced from precipitation changes due to inter-basin discrepancies in HS_{local%}, which is the same as the difference in diabatic heating perturbation between SWM-TRP and SWM-TRPadj. We analyze the steady states by averaging the last 50 days of the SWM experiments. The SWM is substantially less noisy than comprehensive models and the level of internal variability is negligible in the 50-day averages.

The SWM experiments are analyzed in Supplementary Text 1. Specifically, we use SWM-TRP and SWM-TRPadj to verify the circulation responses in amipTRP and amipTRPadj, respectively. The linearity of circulation responses to the diabatic heating perturbations is examined by comparing SWM-TRP minus SWM-TRPadj to SWM-TRP-d-TRPadj.

Quantifying internal precipitation variability

The range of internal precipitation variability in the 30-year amipTRP and amipTRPadj simulations is determined via a Monte Carlo approach ⁴⁰. Using the 2600-year CESM1 pre-industrial control simulation ³⁴, we calculate the difference in precipitation averaged over two randomly selected, non-overlapping 30-year periods. We repeat the above process at each grid point 5000 times to obtain the frequency distribution of such precipitation difference. The 5th and 95th percentiles are used to define the range of internal precipitation variability.

Data Availability

- 476 Model output and observation data can be accessed at the following websites. CMIP6: https://esgf-
- 477 node.llnl.gov/projects/cmip6/. Observed SST: https://pcmdi.llnl.gov/mips/amip/. GPCP:
- https://psl.noaa.gov/data/gridded/data.gpcp.html.

TRMM:

https://www.psl.noaa.gov//data/gridded/data.cmap.html.

480	https://disc.gsfc.nasa.gov/datasets/TRMM_3B43_7/summary.	ERA5:	
481	https://cds.climate.copernicus.eu/cdsapp#!/home.	NCEP/DOE-II:	
482	https://psl.noaa.gov/data/gridded/data.ncep.reanalysis2.html.	JRA-55:	
483	https://jra.kishou.go.jp/JRA-55/index_en.html.		
484			
485	Code Availability		
486	The CESM model code is publicly available at https://www2.cesm.ucar.edu/models/cesm1.2/		
487	Scripts for the analysis and generation of figures are stored at the Zenodo online repository		
488	https://zenodo.org/records/10729735 (ref. 41).		
489			
490	Method-only references		
491	23. Webb, M. J. et al. The cloud feedback model Intercomparison Project (CFI	MIP) contribution	
492	to CMIP6. Geoscientific Model Development 10, 359–384 (2017).		
493	24. Chadwick, R., Douville, H. & Skinner, C. B. Timeslice experiments for unde	rstanding regional	
494	climate projections: applications to the tropical hydrological cycle and Eur	opean winter	
495	circulation. Clim Dyn 1–19 (2017) doi:10.1007/s00382-016-3488-6.		
496	25. Hurrell, J. W., Hack, J. J., Shea, D., Caron, J. M. & Rosinski, J. A new sea sur	face temperature	
497	and sea Ice boundary dataset for the community atmosphere model. J. Cl	imate 21 , 5145–	
498	5153 (2008).		
499	26. Adler, R. F. et al. The Version-2 Global Precipitation Climatology Project (G	PCP) Monthly	
500	Precipitation Analysis (1979–Present). J. Hydrometeor 4, 1147–1167 (200)	3).	

- 501 27. Xie, P. & Arkin, P. A. Global Precipitation: A 17-Year Monthly Analysis Based on Gauge
- Observations, Satellite Estimates, and Numerical Model Outputs. *Bull. Amer. Meteor. Soc.*
- **78**, 2539–2558 (1997).
- 504 28. Huffman, G. J., Adler, R. F., Bolvin, D. T. & Nelkin, E. J. The TRMM multi-satellite precipitation
- analysis (TMPA). in Satellite rainfall applications for surface hydrology 3–22 (Springer, 2010).
- 506 29. Hersbach, H. et al. The ERA5 global reanalysis. Quarterly Journal of the Royal Meteorological
- 507 *Society* **146**, 1999–2049 (2020).
- 30. Kanamitsu, M. et al. Ncep-doe amip-ii reanalysis (r-2). Bulletin of the American
- 509 *Meteorological Society* **83**, 1631–1644 (2002).
- 31. KOBAYASHI, S. et al. The JRA-55 Reanalysis: General Specifications and Basic Characteristics.
- 511 *気象集誌. 第2 輯93,* 5–48 (2015).
- 512 32. Zhang, Y. & Fueglistaler, S. Mechanism for increasing tropical rainfall unevenness with global
- 513 warming. *Geophysical Research Letters* **46**, 14836–14843 (2019).
- 33. Hurrell, J. W. et al. The community earth system model: a framework for collaborative
- research. Bull. Amer. Meteor. Soc. **94**, 1339–1360 (2013).
- 34. Kay, J. E. et al. The Community Earth System Model (CESM) large ensemble project: a
- 517 community resource for studying climate change in the presence of internal climate
- 518 variability. *Bull. Amer. Meteor. Soc.* (2015) doi:10.1175/BAMS-D-13-00255.1.
- 35. Yoo, C., Lee, S. & Feldstein, S. B. Arctic response to an MJO-like tropical heating in an
- idealized GCM. Journal of the Atmospheric Sciences **69**, 2379–2393 (2012).
- 36. Park, M. & Lee, S. Is the stationary wave bias in CMIP5 simulations driven by latent heating
- biases? Geophysical Research Letters 48, e2020GL091678 (2021).

- 37. Chen, R., Simpson, I. R., Deser, C., Wang, B. & Du, Y. Mechanisms behind the springtime
- north pacific Enso teleconnection bias in climate models. *Journal of Climate* **35**, 7691–7710
- 525 (2022).

- 38. Ting, M. & Yu, L. Steady response to tropical heating in wavy linear and nonlinear baroclinic
- 527 models. *Journal of the atmospheric sciences* **55**, 3565–3582 (1998).
- 39. Held, I. M., Ting, M. & Wang, H. Northern winter stationary waves: Theory and modeling.
- 529 *Journal of climate* **15**, 2125–2144 (2002).
- 40. Lu, K., He, J., Fosu, B. & Rugenstein, M. Mechanisms of Fast Walker Circulation Responses to
- 531 CO2 Forcing. *Geophysical Research Letters* **48**, e2021GL095708 (2021).
- 41. He, J., Lu, K., Fosu, B. & Fueglistaler, S. Diverging Hydrological Sensitivity among Tropical
- 533 Basins analysis. Zenodo https://doi.org/10.5281/zenodo.10729735 (2024).